JOURNAL OF MATERIALS SCIENCE 39 (2004) 6885–6899

High-speed testing and material modeling of unfilled styrene butadiene vulcanizates at impact rates

M. S. HOO FATT*, I. BEKAR
Department of Mechanical Engineering, The University of Akron, Akron, OH 44325-3903, USA
E-mail: hoofatt@uakron.edu

High-speed tensile tests were performed on unfilled SBR strip and sheet specimens at room temperature. Uniaxial dynamic stress-extension ratio curves indicated three distinct regions of rate-dependent behavior when strain rates were below 180 s^{-1}, between 180–280 $s^{-1}$and above 280 s^{-1}. With increasing strain rate, the toughness increased in the first region, remained roughly constant in the second region, and decreased in the third region. Time-temperature shift on SBR near the glass transition temperature used to obtain high strain rate tensile strength at room temperature did not give the same results as those found in the impact tensile test. The dynamic toughness was used to predict failure of rubber sheets under impact loads using ABAQUS Explicit. Predicted values of the sheet extension at the onset of failure were within 10% of experimental values.

1. Introduction

This paper is concerned with high-speed rubber testing and the development of material models to predict the deformation and fracture of elastomers under rapidly applied tensile loads. An experimental technique is developed to characterize dynamic material properties of unfilled Styrene Butadiene Rubber (SBR) and find force-extension of SBR sheets under tensile impact loading. High speed tensile test data of SBR are transient or time-domain. This is in contrast to frequency-domain material properties from Dynamic Mechanical Analysis (DMA) tests, i.e., storage and loss modulus. The storage and loss modulus are limited to small strains in which stress is roughly linear with strain and strain rate; DMA tests cannot be used to determine ultimate strength properties, where strains can be greater than 300%. The tensile impact experiment, which will be discussed in this paper, extends dynamic material testing of elastomers to the hyperelastic and nonlinear viscoelastic range. It is a test that will characterize not only deformation but tensile strength of an elastomer at very high strain rates.

High-speed tensile testing on rubber when strain rates are in excess of 10 s^{-1} has been described as early as 1950. Villars [1] reported the tensile strength and breaking extension of several gum and filled vulcanizates extended at strain rates between 100–1000 s^{-1} using a pin on the circumference of a rotating wheel to strike the middle enlarged section of double dumbbell specimens. In 1962, Dannis [2] developed an ultra high-speed tensile test for rubber by dropping weights down a chimney onto an instrumented specimen carriage. Kainradl and Handler [3] reported tensile strength measurements for several vulcanizates at rates up to 600 s^{-1} using drop tower and catapult devices. Greensmith [4] used a tensometer and an autographic method to obtain load-extension curves of filled and unfilled rubber ring specimens extended at rates in the range 0.001–20 s^{-1}. In many of the above-mentioned studies, the rate of extension (strain rate) was not uniform in the specimen and complete stress-extension ratio curves were hard to obtain because computerized data acquisition was not developed at the time. Nevertheless, all of these experimental studies indicate that the tensile strength and breaking extension of rubber can vary appreciably with the rate of extension.

Modern-day high speed tests on elastomers or rubber-like materials are primarily done in compression using Split Hopkinson Pressure Bar [5, 6]. These tests are important in designing shock pads and earthquake isolation bearings [7]. High strain rate tensile data is uncommon because elastomers are not generally used in tension, where they are flexible and weak. Furthermore, many now believe that high speed testing of elastomers is unnecessary since time-temperature superposition, i.e., Williams-Landel-Ferry (WLF) equation [8], can be used to obtain stress-extension ratio curves at high strain rates by shifting stress-extension ratio curves at lower strain rates and lower temperatures. Smith [9] showed that even the tensile strength

*Author to whom all correspondence should be addressed.

and breaking extension of elastomers follow the WLF equation over specified range of strain rates and temperatures. Time-temperature superposition is based on the temperature dependency of the viscoelastic properties of an amorphous polymeric system above its glass transition temperature. The WLF equation is an empirical function describing a constant shift factor or ratio a_T of the mechanical relaxation time at temperature T to its value at a reference temperature T_s. As temperatures decrease below the glass transition temperature, molecular friction increases and allows neighboring chains to support each other. Segmental mobility is severely restricted and time-temperature superposition cannot be applied. A similar restriction on segmental mobility can exist when the elastomer is subjected to ultra high loading rates because characteristic relaxation times may be much longer than the load duration. In this paper, we obtain dynamic stress-extension ratio curves for SBR tensile specimens at strain rates varying between 10–1000 s^{-1}. All experiments are performed at room temperature (25°C) and specimens are loaded until failure. The uniaxial stress-extension ratio curves will be used to develop a hyperelastic model to predict deformation and failure of the rectangular SBR sheets under tensile impact loading.

2. Experimental procedure

The tensile impact apparatus shown in Figs. 1a and b was developed earlier by the authors for obtaining the deformation and fracture characteristics of rubber-like materials under impact rates [10, 11]. This apparatus can be used to obtain both dynamic stress-strain curves of uniaxial strip specimens and force-extension curves of thin sheets and is capable of achieving large strains (up to rupture) and high strain rates (between 10–1000 s^{-1}) in rubber specimens. As shown in Fig. 1a, a Charpy impact pendulum, which is typically used to measure the impact toughness of metals, hits a specially designed slider bar connected to two copper cables. The copper cables are directed around pulleys and attached to guided bases with grips that hold opposite ends of the specimen (see Fig. 1b). The guided bases are allowed to slide freely along steel rails when pulled by the copper cables. Both the slider bar and steel rails are lubricated to reduce friction.

The aluminum guided base shown in Fig. 2 is specially designed to transfer tensile forces from copper cables and carry grips, load cells and displacement transducers. The grips consist of two aluminum plates, which are firmly screwed together when the specimen is placed between them. The edges of the grips are smoothened to prevent them from cutting into the sample. The jaws of the grips are also lined with a thin sheet of rubber to prevent slippage. As shown in Fig. 2, the grips are slotted and held onto the guided bases by a protruding pin, which is in direct contact with the load cells. An ICP Force Sensor Model 208-C01 made by PCB Piezotronics in Depew, New York, is mounted in front of each pin. The load cells are quartz crystal with a resonant frequency of 70 kHz. The linear measurement range for these load cells is ±44.5 N (±10 lb), but they have a useful over-range of ±89 N (±20 lb). The load cells record the impact tensile force when the copper cables pull the guided base. Thus the tensile force on the grip is actually measured as a compressive force as the piezoelectric load cells hit the backside of the grips. Mounted on the same guided bases are two RDP D5 Linear Variable Differential Transformers (LVDTs), which measure extension of the specimen. Each LVDT has a maximum range of ±150 mm.

Data from the load cells and LVDTs are sent to a DATAQ DI-720-USB data acquisition system, which has the ability to collect 250,000 data per second. Since

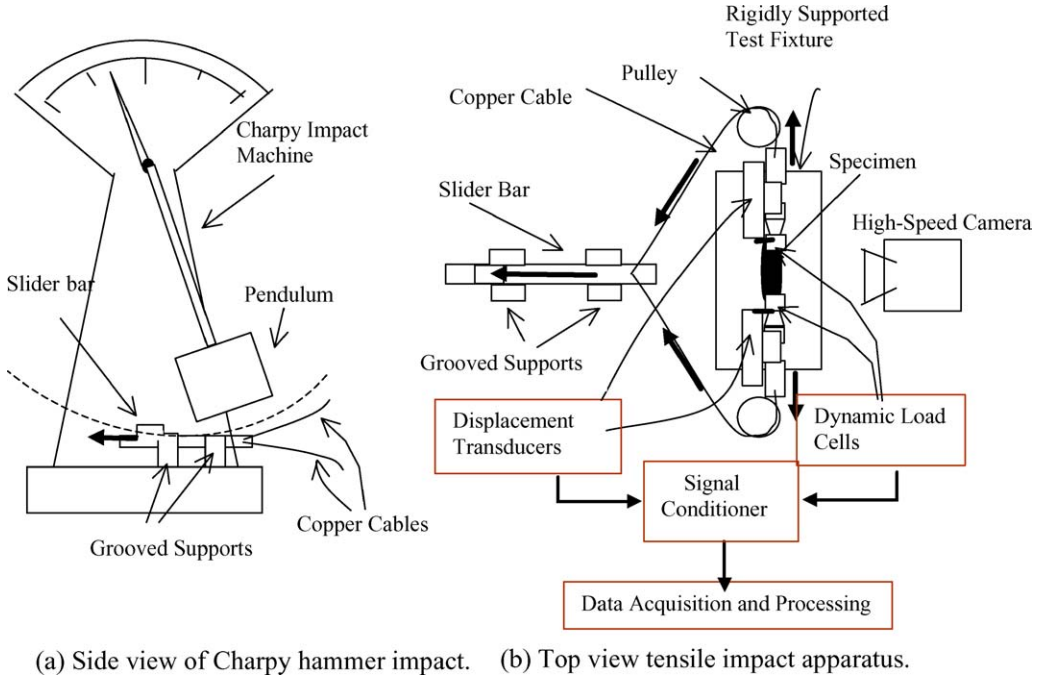

(a) Side view of Charpy hammer impact. (b) Top view tensile impact apparatus.

Figure 1 Schematic diagram of tensile impact test.

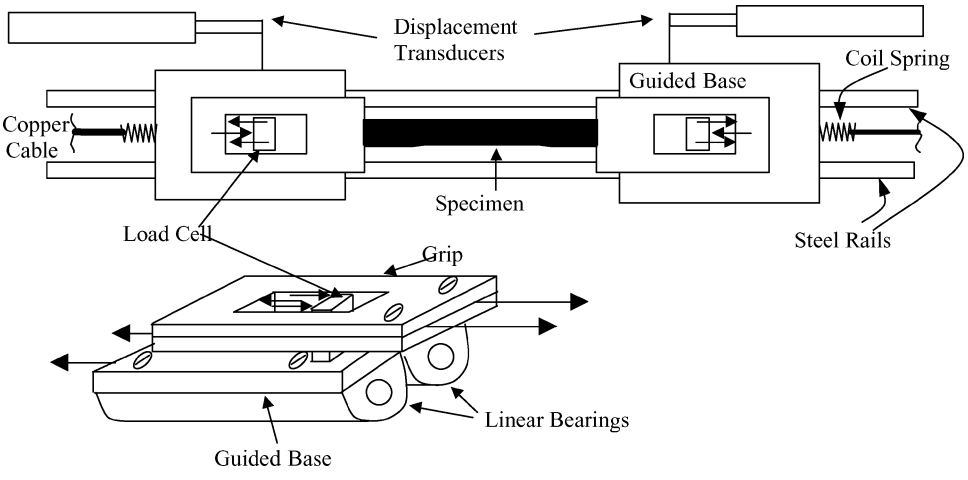

Figure 2 Guided bases.

there are two load cells and two displacement transducers or four channels, each channel can obtain up to 62,500 data points per second, which is deemed sufficient for this type of application. An 8-Channel PCB 482A22 Signal Conditioner is used with the force sensors and two RDP S7AC Transducer Amplifiers are used with the LVDTs before signals from them are sent to the data acquisition system.

Designing the experiment so there are equal grip separation velocities on both sides of the specimen isolates the middle of the specimen so that the fracture process in the center of the rubber sheet can be captured with a high-speed camera. A Photron Ultima APX FASTCAM monocrome camera, which is capable of recording 2,000 frames per second at full resolution and up to 120,000 frames per second at reduced resolution, is used for the high-speed video photography. Halogen light sources, not shown in Fig. 1b, are also used to illuminate the specimen during the video recording.

3. Materials and specimens

The aforementioned apparatus is used to obtain stress-stretch ratio curves of strip specimens and force-stretch response of thin sheet specimens. The specimens are cut from 152.4 mm × 152.4 mm square and 2.54 mm thick sheets of unfilled SBR, which were provided by the Akron Rubber Development Laboratory in Akron, Ohio. The recipe for the SBR is given in Table I. The SBR was cured at 320°F for 11.5 min.

An ASTM D412 strip specimen [12] was chosen to obtain stress-extension ratio curves in the tensile tests. Rectangular strips, 6.35 mm wide and 50.8 mm long, are cut from 2.54 mm-thick SBR sheet using a razor blade. About 12.7 mm of either end of the strip are clamped into the grips so the actual gage length of the specimen is 25.4 mm. Unlike the more common dumbbell specimens, the actual length between grips is the specimen gage length and extensions can be directly measured from the LVDTs.

For the sheet experiments, 50.8 mm × 50.8 mm squares are cut from the SBR sheet so that 12.7 mm from either ends can be clamped into the grips. The sheet is clamped fully along the 50.8 mm length of the specimen. The effective geometry of the sheet specimen is therefore 25.4 mm long × 50.8 mm wide.

TABLE I Recipe for SBR used in the tensile specimens

	SBR 1502	ZnO	Sulfur	St. Acid	MBTS	TMDT
PHr	100	5	2	2	1.6	0.4

4. Tensile test results

Tensile tests on strip specimens are repeated 4–6 times for each drop height to ensure repeatability of the data. Tests in which the specimen either slipped or did not break in the middle are discarded. The transient extension is normalized with respect to the original specimen length (=25.4 mm) to give transient extension ratio λ. The transient force F is divided by the actual cross-sectional area A of the specimen to give transient true or Cauchy stress. Assuming that rubber is incompressible, the true stress σ is given by

$$\sigma = \frac{F}{A} = \frac{F}{A_o}\lambda \tag{1}$$

where A_o is the original specimen cross-sectional area. Transient stress and extension ratio data are then combined to give a single stress-extension ratio curve for a given drop height. This dynamic stress-extension ratio curve is a material property if the entire sample is under uniform stress and constant strain rate.

4.1. Uniform stress state

The ASTM D412 strip specimen retains a uniform uniaxial stress state throughout quasi-static tensile tests because loads are applied very slowly and any point along the sample is in static equilibrium at all times. In our tensile impact test, however, impulsive forces are applied at either ends of the sample and these generate longitudinal stress waves that travel with the speed of sound in the specimen. The rate of applied deformation or velocity at the end of the specimen must be lower than the stress wave speed for the specimen to

be loaded. Furthermore, stress waves must propagate almost instantaneously to the center of the sample for it to be in a uniform stress state. In other words, the wave travel time across half the length of the stretched specimen should be very short compared to the applied load duration. This requirement is particularly difficult to satisfy in an elastomer under tension because the distance over which waves must travel increases as the specimen is stretched.

The longitudinal wave speed or velocity of sound at large strains is given by Gent and Marteny [13] as

$$c = \sqrt{\frac{(1+e)E - \sigma}{\rho}} \tag{2}$$

where E is the instantaneous or tangent modulus, e is the engineering strain and ρ is the density. Under small strain, a linear elastic material is described by $\sigma = Ee$, and Equation 2 reduces to $c = \sqrt{\frac{E}{\rho}}$, which is a more familiar form of the longitudinal wave speed in an elastic medium. Since the tangent modulus and values of the stress and strain that are being propagated are derived from dynamic stress-strain curves, the wave speed and characteristic travel time will have to be calculated after the experiments are conducted. A comparison of the wave travel time to the loading time of the experiment would serve as a check of the validity of the tensile tests.

Another way to check that the sample is being uniformly stretched is to observe the transient deformation of the strip specimen with the high speed camera. A sonic tensile pulse would reveal itself as a neck (reduced cross-sectional area) traveling from the tensile loading end towards the part that has yet to be loaded. An illustration of this in a rubber strip fixed at one end and pulled at high speed at the opposite end can be found in [3]. Fig. 3 shows transient deformations of the strip specimen when the Charpy hammer was released from a drop height of 381 mm. The corresponding transient load and extension at the ends of the sample in this experiment are given in Fig. 4. The video was taken with the high-speed video camera set at 50,000 frames per second. Thus images were taken every 0.02 ms. The total time of the experiment is about 20 ms. The images in Fig. 3 indicate that the axial strain is uniformly distributed throughout the specimen at all times during tests. Either the sample reached steady-state condition due to very rapid wave propagation or the tensile load increments are so small that the prior and past deformations are indistinguishable. For all practical purposes, the specimen is in a uniform stress state.

4.2. Constant strain rate

The transient forces and extensions shown in Fig. 4 are similar to those obtained at other drop heights. The tensile force on the cables from the Charpy hammer is so high that extensions increase at a fairly constant rate after a small transition time. The specimen is not only uniformly stressed but it is also deforming under constant strain rate. Engineering strain-time plots for various drop heights are shown in Fig. 5 and the slopes of these graphs are used to find the strain rate of each experiment. The strain rate of the sample is defined as the time rate of change of the engineering strain. The strain rates of the experiment remain fairly constant after an early transient, which corresponds to low strain values. For instance, at the lowest drop height, the initial transient occurs when the engineering strain is less than 25% and remains constant when strain rate is between 25–250%. As the drop height increases, the lower limit of the constant strain rate region approaches zero. At the highest drop height, for instance, the strain rate becomes constant when strains are greater than 5%. Since we are interested in full stress-strain curves where strains are a few hundred percent, we can ignore the initial transient and assume that the strain rate is constant for all strains. Table II gives calculated strain rates in the specimen for each drop height in the experiments. These strain rates will be used to reference stress-stretch ratio curves in the next section.

4.3. Dynamic stress-extension ratio curves

As mentioned earlier, extension ratio-time data are combined with the corresponding stress-time data to produce Cauchy stress-extension ratio curves as shown in Fig. 6. Quasi-static tensile test results on the same specimen using an Instron universal testing machine are also provided in Fig. 6 for comparison. Points Ⓐ at 180 s^{-1} and Point Ⓑ at 280 s^{-1} in Fig. 6 separate three regions of rate-dependent deformation and fracture behavior. We identify three phases of deformation and fracture labeled Regions 1, 2 and 3 in Fig. 6. The corresponding fracture surfaces for these three regions are given in Fig. 7. The appearance of dull-to-shiny surfaces in Regions 1–3 suggests that crack velocity increase with increasing strain rate. We next compare the wave propagation speed to the grip velocity and the wave travel time for stresses at large (breaking) strains to the load duration as a check of the validity of the material tests.

4.4. Longitudinal wave speed at large strain

The dynamic stress-extension curves are roughly linear in the large strain region. The gradient of this line or tangent modulus in the large strain region varies noticeably with strain rate in Region 2 (between Points Ⓐ and Ⓑ), but it is almost insensitive to strain rate in Region 1 and a constant value in Region 3. The speed of a tensile stress large enough to break the specimen will not only depend on this modulus but also on the stress and strain at the breaking point. Substituting $e = \lambda - 1$ into Equation 2 gives the following expression for the tensile wave speed at the breaking point c_b in terms of the breaking extension λ_b and tensile strength σ_b:

$$c_b = \sqrt{\frac{E_b\lambda_b - \sigma_b}{\rho}} \tag{3}$$

where E_b is the tangent modulus at the breaking point. The mass density of the SBR used in our experiments was measured as $\rho = 1045$ kg/m^3. The tangent

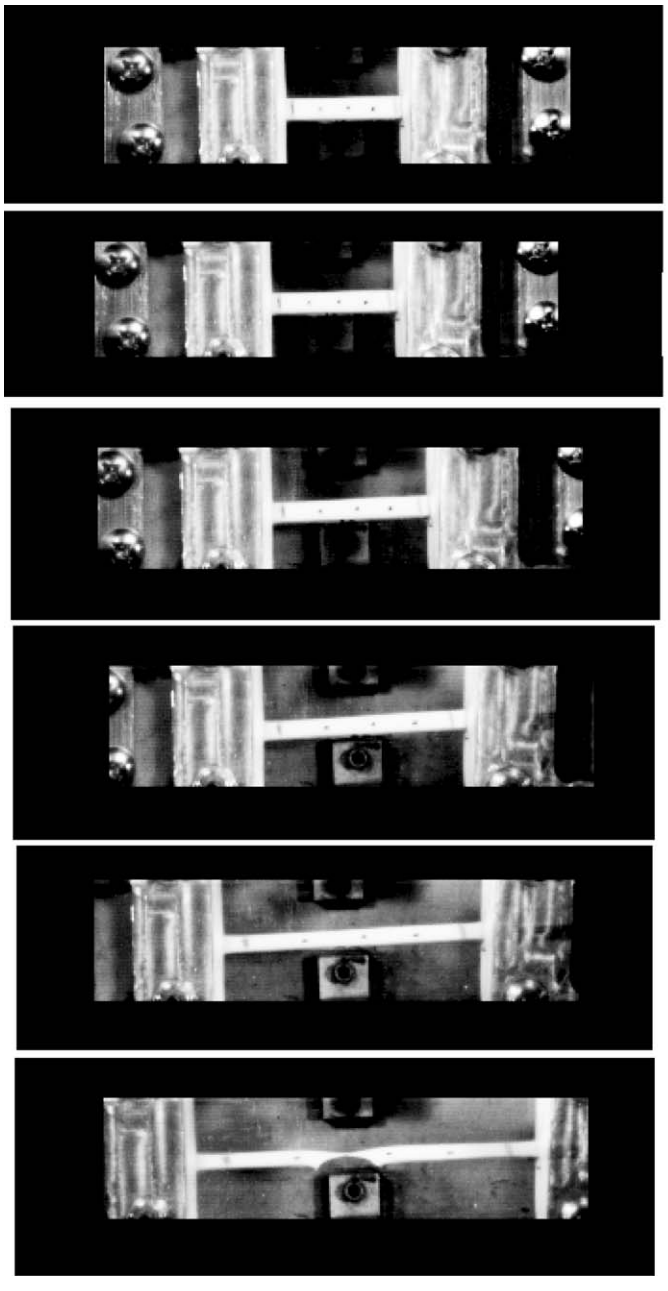

Figure 3 Snapshots of tensile specimen during test at 381 mm drop height.

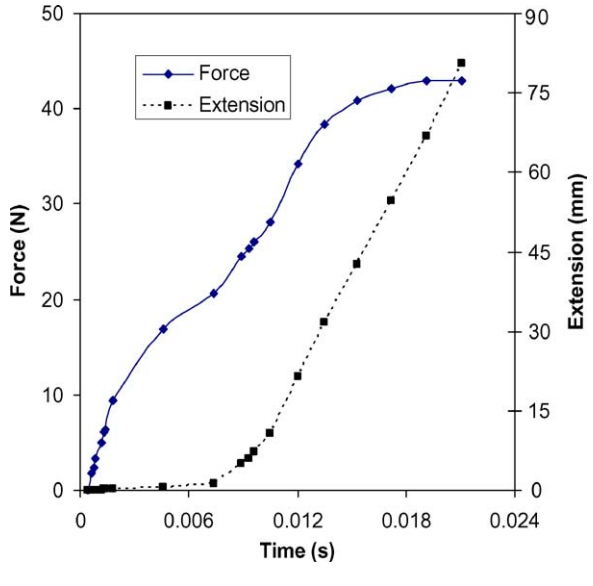

Figure 4 Transient force and extension in 381 mm-drop height test.

modulus at failure, breaking extension and tensile strength for selected strain rates are given in Table III and from these, wave speeds at breaking are calculated. The wave speed at the tensile strength varies between 20–43 m/s. As indicated in Table III, the corresponding grip velocity in each tension test at each loading rate is always less than the wave propagation speed. If this were not the case, the tensile wave would not be able to propagate through the specimen.

Tensile waves need to travel only half of the current length of the specimen since the specimen is being loaded at both ends. Thus the travel time of the breaking stress t_b is given by

$$t_b = \frac{\lambda_b l_o}{2c} \tag{4}$$

where $l_o = 25.4$ mm is the initial specimen gage length. This is the longest wave travel time since it is calculated for a fully stretched specimen. Other stresses below the

TABLE II Strain rates associated with drop heights

Drop height (mm)	25.4	50.8	76.2	101.6	127	254	381	508	635	762	889
Strain rate (s^{-1})	13	23	40	114	180	230	250	280	390	420	480

TABLE III Comparison of longest wave travel time and load duration

Strain rate (s^{-1})	Breaking extension ratio λ_b	Tensile strength σ_b (MPa)	Tangent modulus at fracture E_b (MPa)	Wave speed c_b (m/s)	Grip velocity (m/s)	Wave travel time t_b (ms)	Load duration (m/s)
13	3.45	6.1	2.32	42.68	0.17	1.0	330
114	4.15	8.8	2.34	29.53	1.4	1.8	75
180, Ⓐ	4.7	10.8	2.61	37.47	2.3	1.6	53
250	4.15	11.0	2.76	20.84	3.2	2.5	22
280, Ⓑ	3.9	11.0	3.35	44.45	3.6	1.1	15
390	3.52	10.0	3.35	41.41	5.0	1.1	8.4
480	2.25	5.8	3.35	40.78	6.1	0.7	3.3

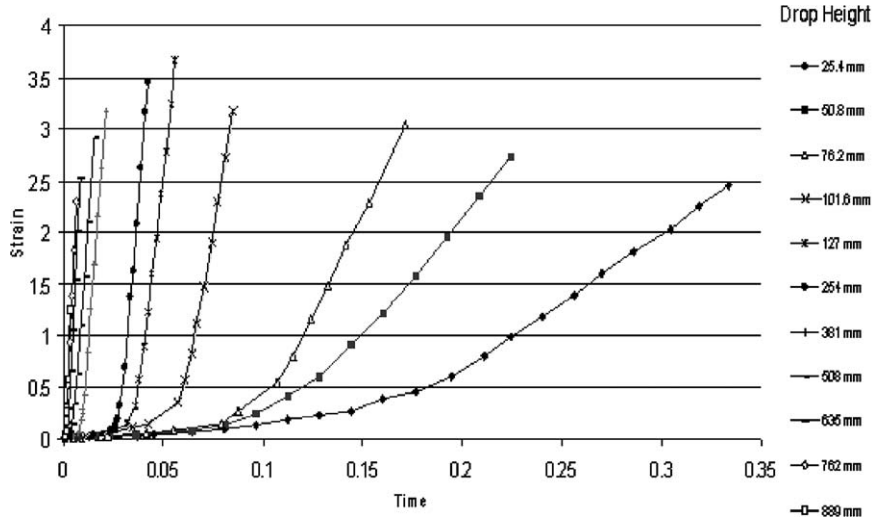

Figure 5 Engineering strain-time graphs for SBR corresponding to different pendulum drop heights.

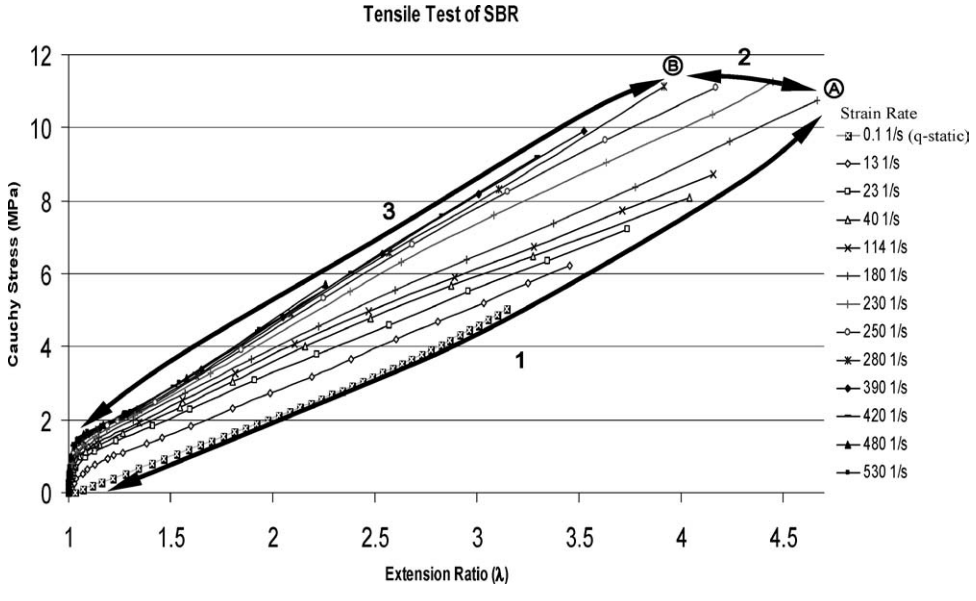

Figure 6 Cauchy stress-extension ratio curves at varying strain rates.

tensile strength would reach the middle of the sample in shorter times. The calculated wave travel times are compared to load durations in Table III. In all cases, the wave travel time is lower than the load duration, but at strain rates above 280 s^{-1} (Region 3), we are approaching a limit on the dynamic tests. In order to achieve higher strain rates, the specimen gage length must be reduced. Such is the case in the experiment performed at 530 s^{-1} (see Fig. 6), where the gage length is reduced to 12.7 mm.

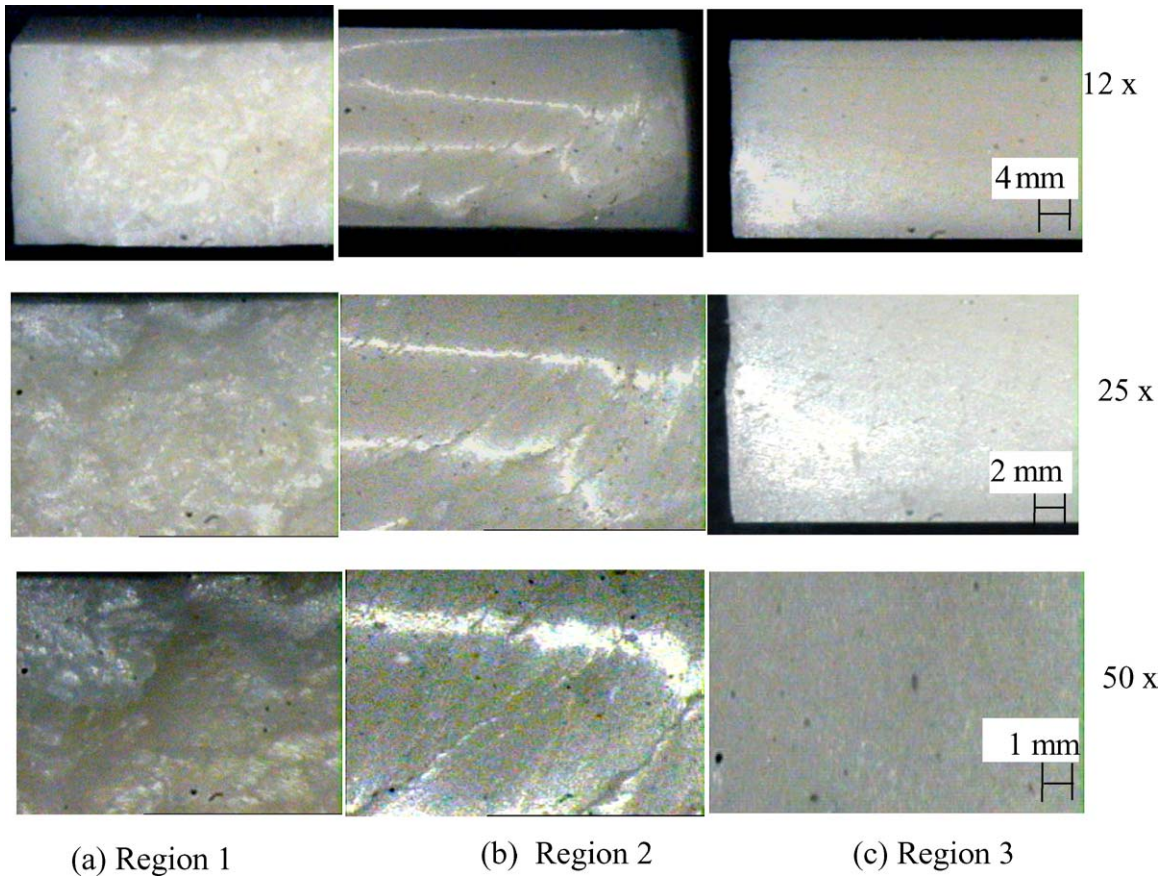

Figure 7 Fracture surface of tensile specimen in three phases.

4.5. Rate-dependent behavior in Regions 1, 2 and 3

In Region 1, the initial modulus, yield stress, tensile strength and fracture strain increase with increasing strain rate. In Region 2, the final modulus and fracture stress increase and the fracture strain decreases as the strain rate increases. Finally, in Region 3, the modulus of rubber is virtually independent of strain rate and all stress-stretch ratio curves appear to follow a master or limiting curve. Thus the deformation of rubber at very high rates can be predicted using hyperelasticity if a strain energy potential function for SBR can be defined in Region 3. We will explore this in Section 6, where we use hyperelasticity to predict the deformation and fracture of rubber sheets under tensile impact loads.

The occurrence of the above three regions can be easily understood when one considers the composition and morphology of an elastomer such as SBR. Styrene Butadiene Rubber is composed of long chain molecules of carbon-hydrogen monomers with occasional butadiene and styrene units. Alfrey [14] referred to these as convolutions, curls and kinks. The long chains intertwine to form entanglements (knots) and are crosslinked with sulfur. Molecules reptate, or slide, except at the entanglements and crosslinks when the elastomer is under an applied stress. Relaxation, which is intermolecular slippage accompanied by some reversible breaking or swapping of bonds, takes place during this time. The various types of slippage are distinguished by different relaxation times because they occur over different length scales. Relaxation on a local scale involves relatively rapid de-orientation of the kinks in the molecular chains. Relaxation on a long-range scale involves very slow rearrangements of the convolutions with respect to each other. The relaxation time on the local scale is very short and the relaxation time on the long-range scale is long. Between these two length scales, there is a wide and continuous range of spatial scales and relaxation times. As the loading rate increases, the time for relaxation processes decreases and some relaxation mechanisms do not occur. This accounts for rate-sensitivity of the modulus, tensile strength and fracture strain of our SBR specimen.

In Fig. 6, one can see that in Region 1, the initial modulus increases significantly with increasing strain rate but the variation of the final modulus with strain rate is not as strong. In Region 2, however, the increase in the final modulus with increasing strain rate becomes noticeable while variation of the initial modulus is not as significant. In Region 1, long-range relaxation is consecutively ceasing to occur as the time of the experiment decreases. During Region 2, none of the long-range relaxation processes can occur during the very short loading times. Variation of the final modulus in Region 2 is therefore due to a lack of relaxation on a local scale. In Region 3, virtually no relaxation occurs and deformation can be described by a single stress-extension ratio curve.

4.6. Failure envelope

The end points in Fig. 6 represent a failure envelope for SBR under high strain rates. A similar failure envelope for SBR-I was almost obtained by Smith [9] using time-temperature shift. Smith performed fourteen sets of constant strain-rate tensile tests to find the ultimate tensile properties of unfilled vulcanized SBR-I over temperatures ranging from—67.8 to 73.3°C. Each set of experiments was done at a constant temperature and strain rates varying between $0.158 \times 10^{-3} - 0.158\ s^{-1}$. Smith used time-dependent data on the tensile strength σ_b and stretch ratio at break λ_b at different temperatures T to show that they were in agreement with the WLF. Specifically, Smith used the following equation to determine the shift factor a_T:

$$\log a_T = \frac{-8.86(T - T_s)}{101.6 + T - T_s} \tag{5}$$

where $T_s = 263$ K is the reference temperature. He then constructed a failure envelope by plotting $\log \sigma_b\, 263/T$ against $\log(\lambda_b - 1)$, as shown in Fig. 8. This failure envelope is independent of strain rate and temperature since an increase in strain rate or decrease in temperature shifts the rupture point counterclockwise around the envelope.

All of Smith's test data fall on a curve that can be predicted by time-temperature shift (see solid curve in Fig. 8), even though there is some scatter in the upper right-hand region of the graph. Smith's failure envelope indicates that the rupture process is viscoelastic in nature since it can be predicted from time-temperature superposition. However, the scatter of data in the upper transition region, which corresponds to high strain rate and/or low temperature, suggests that time-temperature superposition may be inapplicable to materials that experience significant inertial forces or wave propagation.

The failure envelope in Fig. 8 resembles the lower half of our failure envelope in Fig. 6. Smith's experiments did not reveal Region 3 of Fig. 6 or the other transition point at Ⓑ because this regime was out of his experimental range. Recall that the highest strain rate in Smith's experiments was only $0.158\ s^{-1}$.

In order to make a rough quantitative comparison of both failure envelopes for SBR, the median strain rate ($\approx 10^{-2}\ s^{-1}$) of each set of Smith's experiments at constant temperature was shifted to a value at room temperature. The calculated strain rates at room temperature are listed next to the appropriate set of experiments in Fig. 8. The maximum elongation at break in Smith's experiment, which occurred at −34.4°C, corresponds to a strain rate of about $10^2\ s^{-1}$ at room temperature. This is about the same order of magnitude as the strain rate at point Ⓐ. We thus conclude that time-temperature shift can be accurately used to describe data in Region 1. However, Smith's data shifted to room temperature does not agree with our experimental results in Region 2 since it would indicate that the tensile strengths for SBR at 10^3 and $10^4\ s^{-1}$ are higher than it would be at $10^2\ s^{-1}$. Our dynamic tensile test results indicate that they should be much lower. The tensile strength at $420\ s^{-1}$, for instance, is 9.3 MPa, and it decreases from this value with increasing strain rate.

Evidently, molecular mobility is reduced at temperatures near the glass transition temperature (≈ -40°C from DMA test on our SBR). The time-temperature shift, which we used to calculate strain rates at room temperature, does not give realistic values for the tensile strength and elongation at break because it assumes that all molecular chains of the elastomer are mobile so that viscosity and density can vary substantially with temperature [8]. When an elastomer is near the glass transition temperature, not all parts of the molecular

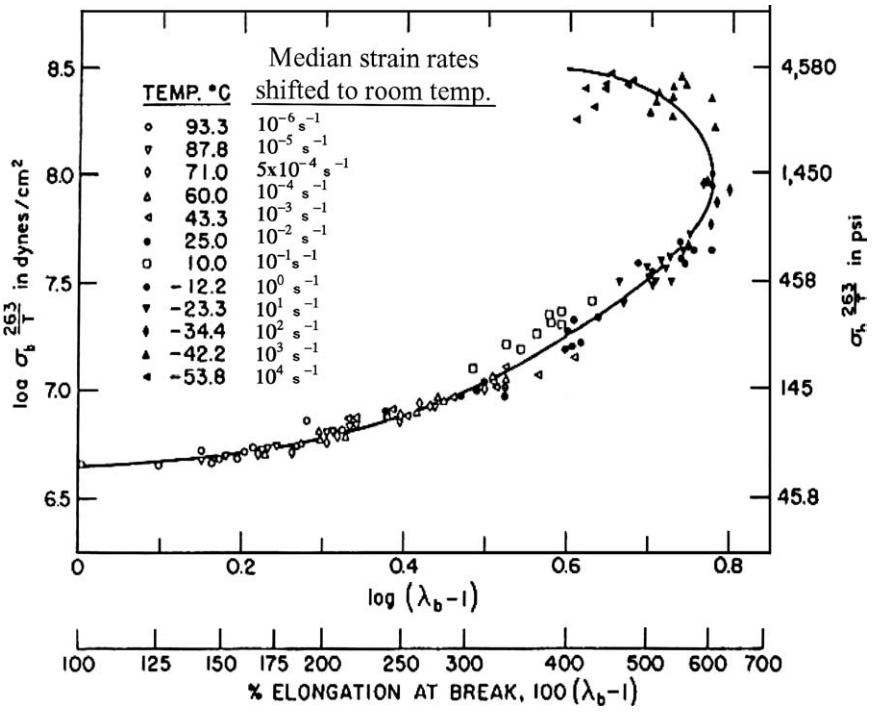

Figure 8 Failure envelope for SBR-I (taken from Ref. [9]).

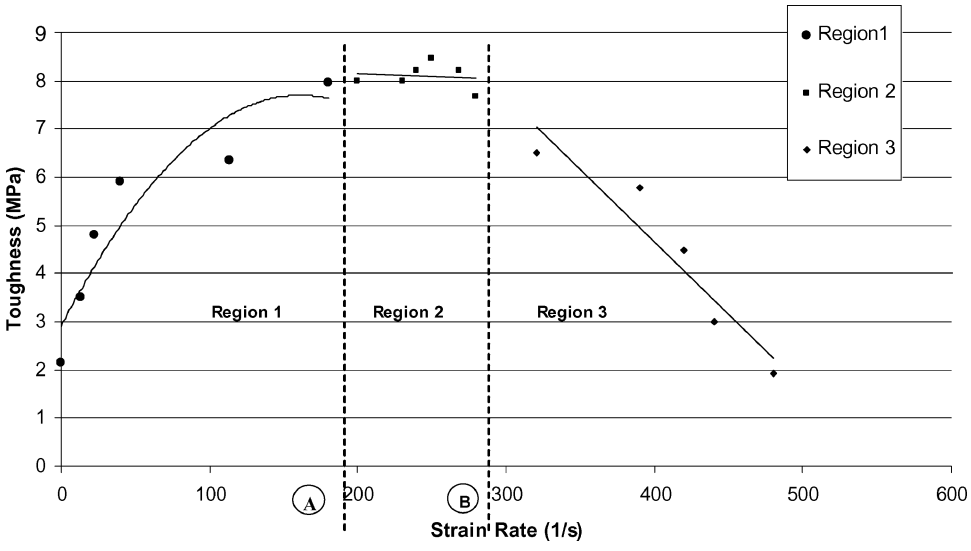

Figure 9 Variation of SBR toughness with strain rate.

chains are mobile and perhaps shift factors must be adjusted.

4.7. Dynamic toughness

Rupture properties of rubber can be described in terms of toughness, i.e., the strain energy per unit volume of material necessary to cause fracture or the area under an engineering stress-strain curve of a uniaxial tensile specimen stretched up to its breaking point. Results from the high strain rate tensile tests were plotted in terms of engineering stress and strain and a dynamic toughness was calculated by finding the area under each curve. Fig. 9 shows how the toughness varies with strain rate. In Region 1, the toughness increases with increasing strain rate. The toughness is roughly constant with increasing strain rate in Region 2, but the toughness decreases with increasing strain rate in Region 3. The fact that the toughness decreases as the strain rate increases is particularly important for rubber components subjected to transient loads because it means that they would have a greater propensity to break than when under quasi-static loading conditions. The next section describes sheet experiments, which show how rubber fractures under high-speed loading. This experiment is done to see if the dynamic toughness of SBR can be used as a fracture parameter to predict failure of rubber components under high strain rate conditions.

5. Results from plate experiments

Fig. 10 shows the resulting force-extension response of the SBR sheets at different loading rates. In this figure, the loading rate is defined as the ratio of grip velocity to original height of the sheet. All of the force-extension curves indicate instabilities before final fracture. Comparison of the high-speed video images and the transient load/displacement measurements show that all of the force-stretch graphs become unstable at the onset of fracture in the center of the plate. Figs. 11a–d show

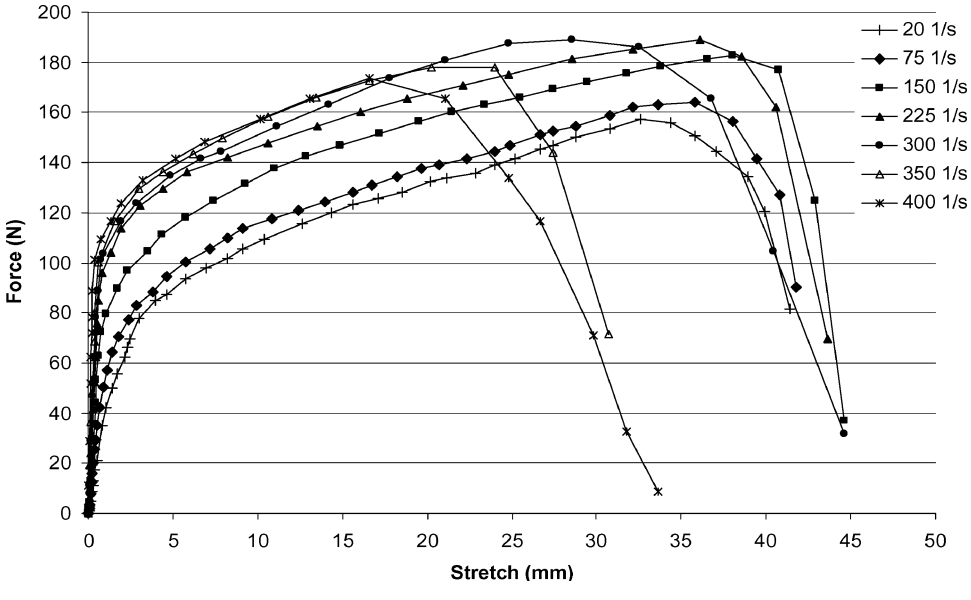

Figure 10 Force-extension curves for SBR sheet at different loading rates.

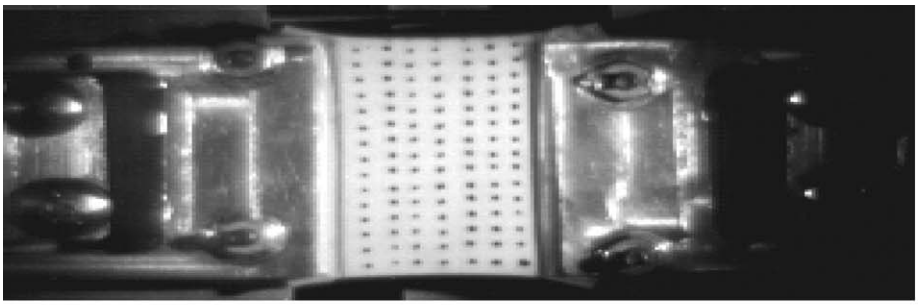

(a) Beginning of the experiment, t=0 msec.

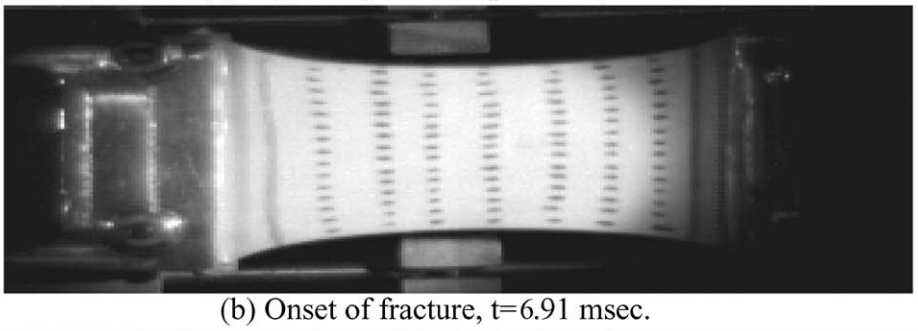

(b) Onset of fracture, t=6.91 msec.

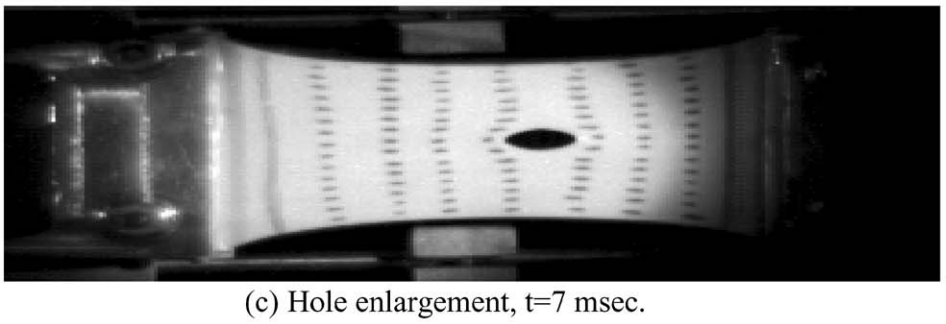

(c) Hole enlargement, t=7 msec.

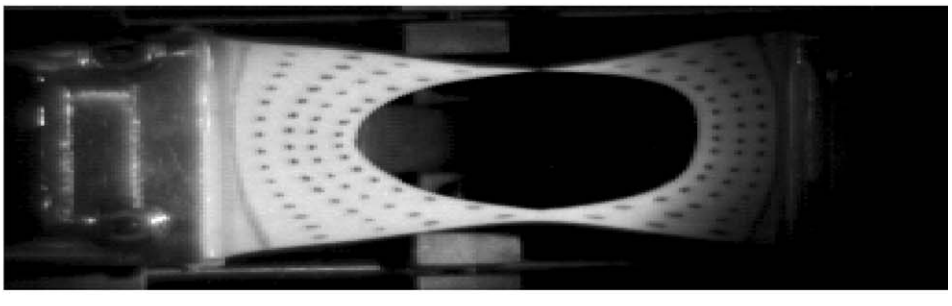

(d) Final fracture, t=13 msec.

Figure 11 Images of SBR sheet subjected to105 s^{-1} loading rate.

the images during the experiment at the 105 s^{-1} loading rate. The specimen deforms without any sign of fracture until the maximum load is reached and a hole suddenly initiates at the center of the sheet (see Fig. 11b). This hole enlarges until the entire specimen breaks in two parts as shown in Figs. 11c and d. As the hole enlarges, the force drops in the force-extension curve.

Since the deformation rate in the sheet is not uniformly distributed, as was the case in the tensile specimen, different regions in the sheet can experience rate-dependent behavior described as Region 1, 2 or 3. However, when the loading rates are greater than 280 s^{-1}, every point in the sheet should be in Region 3. Material would fail when the strain energy density reaches the dynamic material toughness that is appropriate at that particular strain rate (or combination of strain rates). In the next section, we will show how the dynamic toughness of SBR in Fig. 9 can be used to predict damage initiation in rubber sheets when they are subjected to loading rates in excess of 280 s^{-1}.

6. Predicting damage initiation of rubber sheets with FEA

A finite element program using ABAQUS Explicit [15] is used to calculate the dynamic response of the rubber sheet in the experiments and, in particular, the strain energy density and strain rate at every point in the sheet during deformation. Due to symmetry about centerlines shown in Fig. 12, only a quarter of the sheet is modeled. Displacements at the bottom centerline are fixed in the 2-direction but can move along the

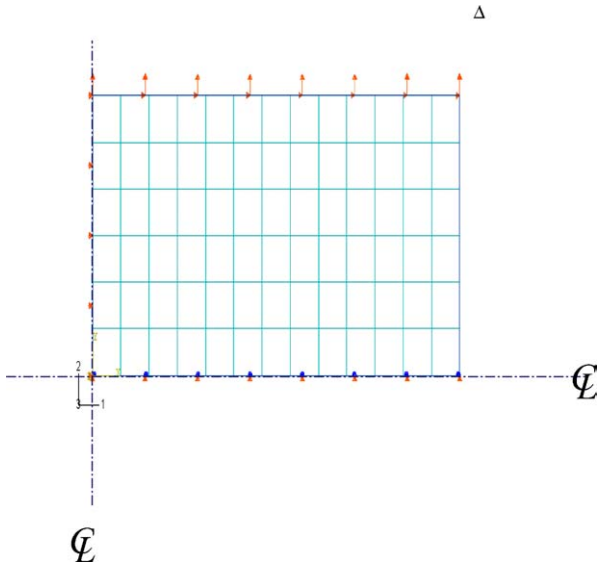

Figure 12 FEA mesh of upper right-hand quarter of SBR sheet.

1-direction freely. At the left centerline, displacements are fixed in the 1-direction and free in the 2-direction. Rotations about the 3-direction are fixed at both centerlines.

Continuum, plane stress, 4-node bilinear, and reduced integration elements (CPS4R) are chosen because they give the best hourglass control. A parametric study on the size of the mesh was done and it was determined that 78 elements were sufficient to accurately simulate the sheet deformation response [11]. Transient displacement, i.e., the extension-time measurement from the LVDTs, is applied to the top boundary of the quarter model. Although the sheet could also be viewed as loaded by transient tensile forces, the transient loading functions have instabilities. The displacement amplitude is defined to exactly replicate the deformation during the experiment. The time step of the transient displacement is 7.13 ms, the time of the experiment. Automatic time increment option with no mass scaling is used. The automatic time increment scheme in ABAQUS Explicit uses an element-by-element stable time estimator to determine the time increment and requires no user intervention. It offers a good balance between analysis stability and turnaround time.

6.1. The hyperelastic function in Region 3

Several strain energy potential forms are considered to describe hyperelastic behavior of SBR in Region 3 of Fig. 6. As shown in Fig. 13, only the second-order polynomial and the third-order Ogden could describe the very stiff initial modulus in the glassy region. The material's uniaxial stress-stretch ratio ($\sigma - \lambda$) curve is modeled as an incompressible material with the following third-order Ogden strain energy potential function:

$$\sigma = 2\frac{\mu_1}{\alpha_1}\left(\lambda^{\alpha_1} - \lambda^{-\frac{1}{2}\alpha_1}\right) + 2\frac{\mu_2}{\alpha_2}\left(\lambda^{\alpha_2} - \lambda^{-\frac{1}{2}\alpha_2}\right) + 2\frac{\mu_3}{\alpha_3}\left(\lambda^{\alpha_3} - \lambda^{-\frac{1}{2}\alpha_3}\right) \quad (6)$$

where $\mu_1 = -10.5$ MPa, $\mu_2 = 17.3$ MPa, $\mu_3 = 6.8$ MPa, $\alpha_1 = 7.7$, $\alpha_2 = -13.5$ and $\alpha_3 = -11.4$. Bekar [11] found that taking higher than third-order Ogden forms does not improve the waviness of these curves, which is sometimes viewed as material instabilities.

The very steep initial modulus followed by material softening in Region 3 is characteristic of power-law hardening materials and not characteristic of a quasi-static stress-stretch ratio curve of an elastomer. Under quasi-static loading, there is usually an upturn in the stress-stretch curve in the large strain region when the molecular chains become nearly fully stretched. Both the Arruda-Boyce [16] and Gent [17] energy potential functions are able to predict this upturn for the uniaxial stress state, while polynomial, reduced polynomial and Ogden potential forms can only approximate values at the upturn when higher order terms are taken into account. As shown earlier, these strain energy potentials, which are based on quasi-static test results, become unstable in the large strain region when they are applied to the hyperelastic curve in Region 3.

6.2. Comparison of load-extension response

The numerical prediction of the force-extension response of the sheet for the 400 s^{-1} loading rate experiment is compared to the experimental results in Fig. 14. The numerical simulation predicts the load-extension curve very well up to point C, i.e., the point of crack initiation. Past point C, the FEA program predicts a stable load-extension because a fracture criterion has not been introduced in the FEA program.

It is assumed that the strain energy density at a material point in the sheet must have reached a critical value at the time of failure. In order to locate the site of damage initiation, the strain energy density in the sheet was monitored in the FEA program. Figs. 15a–d show the contour plots of the strain energy density at consecutive sheet extensions. They are largest at the center of the sheet and the edge of the clamp because the material is highly constrained at both locations. Crack initiation at the sheet center and crack growth as a hole in the sheet center has been confirmed by high-speed videos. Tearing at the clamped edges is also detected in the high-speed video but only after the hole initiates at the sheet center. To predict whether failure initiates in the sheet center or the edge of the clamp, one would need to monitor both the strain energy density and the strain rate. It is found that the longitudinal strains (and strain rates) are higher at the center of the sheet than they are at the clamped edges and this explains why a hole in the center of the sheet occurs before tearing at the edge of the clamp.

6.3. Dynamic failure criterion

The dynamic toughness of SBR shown in Fig. 9 is a rate-dependent material property that can be used to describe failure at a point, specifically a point in a uniaxial stress state. A necessary requirement for failure at

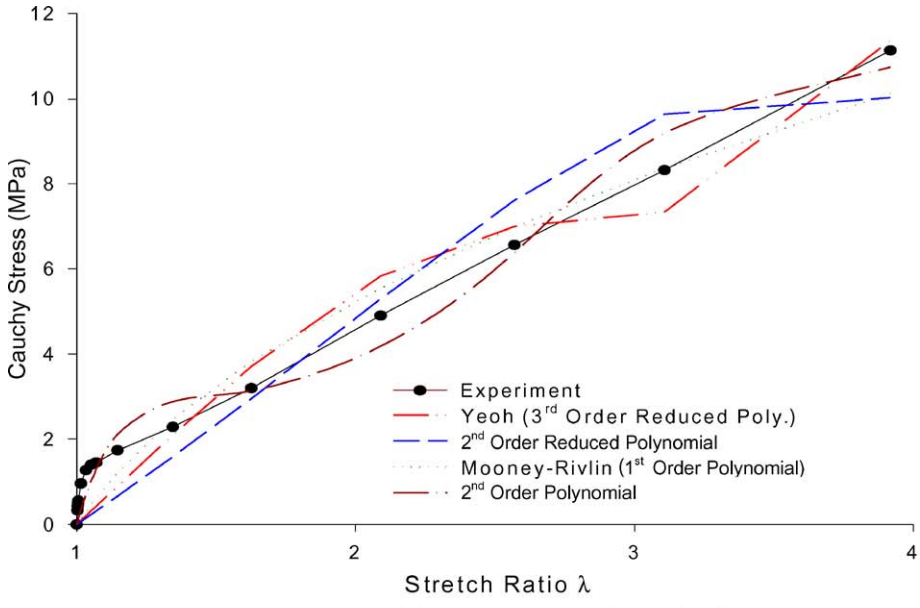

(a) Polynomial and reduced polynomial forms.

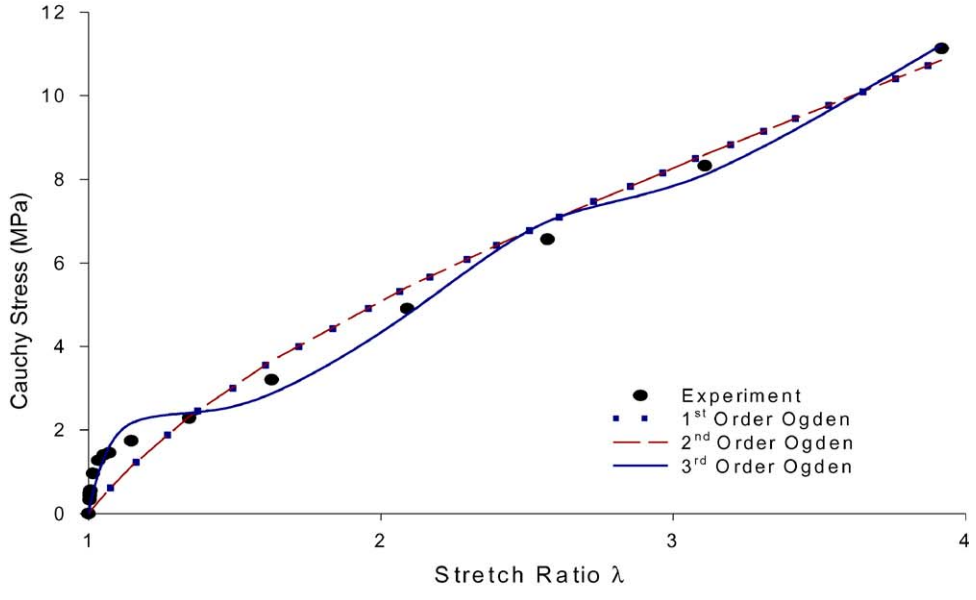

(b) Ogden forms.

Figure 13 Uniaxial stress-stretch ratio curves for different strain energy potentials.

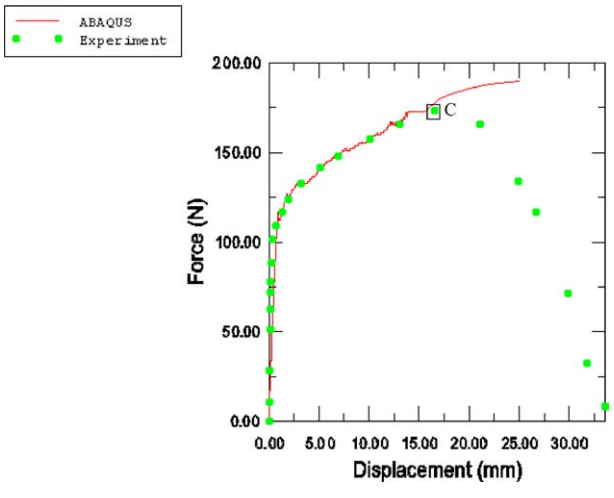

Figure 14 Load-extension response of sheet at 400 s^{-1} loading rate.

a material point in a structure is that the strain energy density is equal to the material toughness at a particular strain rate. However, structures are, in general, multiaxial and there are three principal strain rates associated with each material point. To predict failure of a rubber sheet, which is biaxial, one has to find a strain rate that is invariant to both the uniaxial tensile specimen and the sheet. We propose to relate toughness to the first invariant of the left Cauchy-Green strain rate tensor $\dot{I}_1$, defined as

$$\dot{I}_1 = \dot{\lambda}_1^2 + \dot{\lambda}_2^2 + \dot{\lambda}_3^2 \tag{7}$$

where λ_i for $i = 1, 3$ are extension ratios and the dots denote time derivative.

In the tensile test, the longitudinal strain rate is really only one of three principal strain rates that can be de-

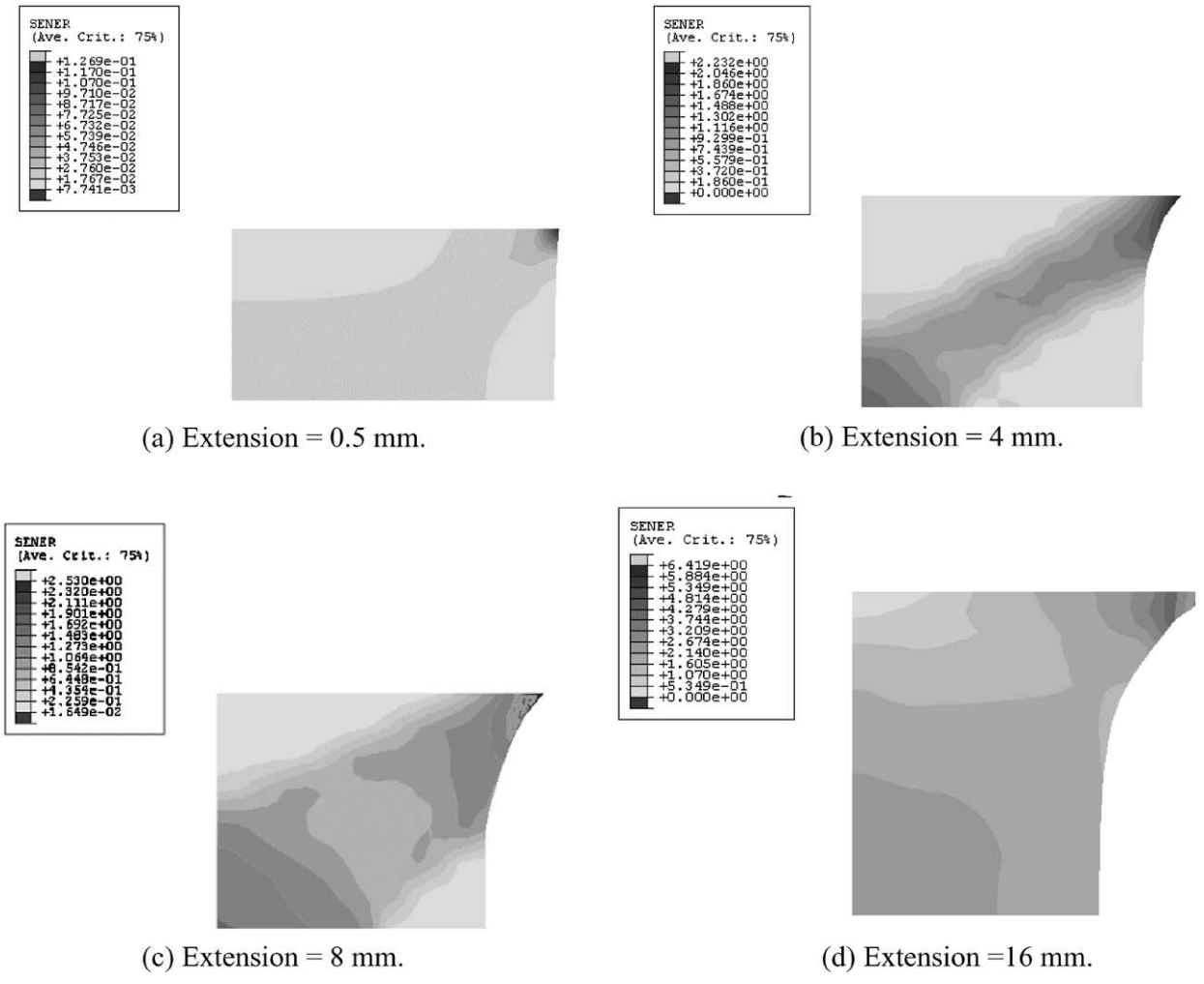

Figure 15 Strain energy density distribution in the sheet at 400 s^{-1} loading rate.

fined in the strip specimen. For incompressible rubber,

$$\lambda_1\lambda_2\lambda_3 = 1 \tag{8}$$

Thus in the tensile test where the 2-direction is longitudinal, $\lambda_2 = \lambda$ and

$$\lambda_1 = \lambda_3 = \frac{1}{\sqrt{\lambda}} \tag{9}$$

The above equation is used to evaluate the other two principal extension ratios in the tensile tests and like the longitudinal strain rate in each tensile test, the time rate of change of $\lambda_1 = \lambda_3$ is found to be roughly constant as the specimen stretches. A constant value of $\dot{I}_1$ could therefore be defined for each material test. This is plotted as a dashed line in Fig. 16.

In the sheet experiments, we also use the incompressibility requirement to determine the extension ratio associated with the through-thickness direction of the sheet,

$$\lambda_3 = \frac{1}{\lambda_1\lambda_2} \tag{10}$$

The above extension ratio cannot be determined directly from the FEA program since we are using two-dimensional, plane stress elements. Only λ_1 and λ_2 can be obtained directly from the ABAQUS Explicit program. The time rates of change of all three principal elongation ratios are calculated to obtain $\dot{I}_1$ at the center element. The strain energy density and first invariant of the extension ratio rate at the center element are calculated at each time step and these values are compared to the variation of toughness with $\dot{I}_1$ for the 400 s^{-1} loading rate sheet experiment in Fig. 16. The variation of strain energy density at the center element and toughness with $\dot{I}_1$ are shown as solid and dashed lines respectively in Fig. 16. Failure of the center element occurs when the strain energy density is 4.54 MPa and $\dot{I}_1 = 158,652\ s^{-2}$. These two values were obtained at a sheet extension of 17.6 mm, which compares very well to an experimental value of 16.5 mm for the sheet extension at the onset of failure.

TABLE IV Use of dynamic toughness to predict onset of failure of SBR sheets

Loading rate (s^{-1})	First invariant of strain rate (s^{-2})	Strain energy density at fracture = toughness (MPa)	Extension at fracture	
			Predicted value (mm)	Test (mm)
300	125,500	6.20	29.5	28.0
350	131,600	5.80	26.0	24.0
400	158,652	4.54	17.6	16.5

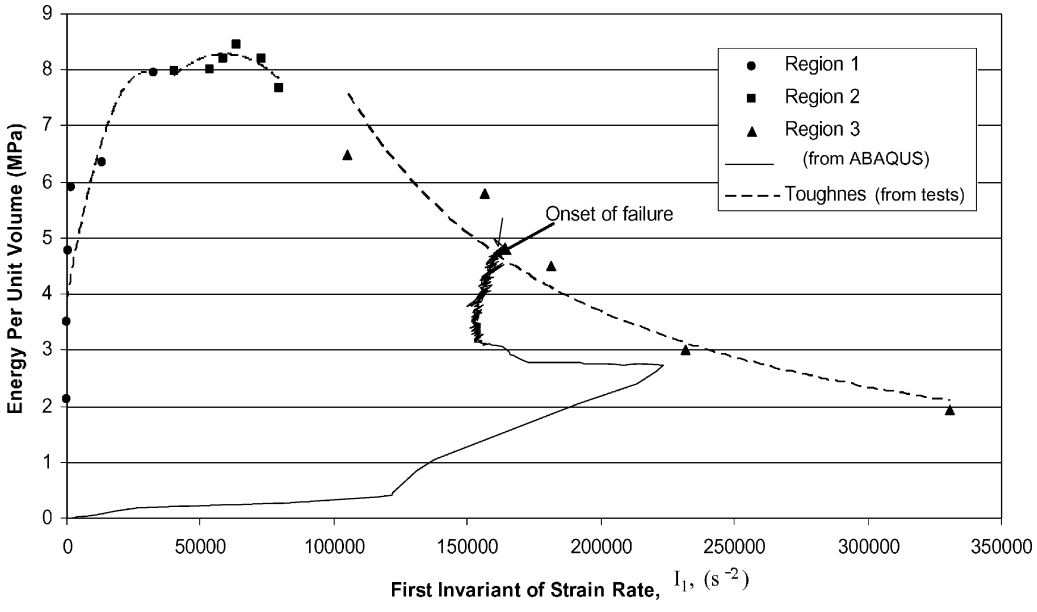

Figure 16 Comparison of strain energy density (from ABAQUS) and toughness (from tests) as a function of the first invariant of the extension ratio rate at the center element.

The failure criterion has been applied to two other loading rate experiments and the results are shown in Table IV. In all three cases, the predicted sheet extension at the onset of failure over-predicted experimental values by less than 10%. We thus conclude that the dynamic toughness can be used as a fracture parameter of SBR provided that it is operating in Region 3. It remains to be seen whether the dynamic toughness can also be used as a fracture parameter for SBR in Regions 1 and 2 in future research. As mentioned earlier, the stress-extension ratio curves are rate-dependent and both deformation and fracture are related to viscoelastic or relaxation mechanisms. Hyper-viscoelastic relations will therefore be developed in the future.

7. Conclusions

High-speed tensile tests were performed on unfilled SBR strip and sheet specimens at room temperature using a newly proposed tensile impact apparatus. This apparatus uses the Charpy impact hammer to hit a slider bar connected to copper cables, which apply sudden tensile loads on opposite ends of the specimen. Dynamic stress-extension ratio curves up to failure were obtained for SBR at strain rates in the range 13–530 s^{-1} and three distinct regions of rate-dependent deformation and fracture behavior were identified. In Region 1, corresponding to strain rates below 180 s^{-1}, the initial modulus, tensile strength and breaking extension increased as the strain rate increased. Between strain rates of 180 and 280 s^{-1} was Region 2, where the initial modulus and tensile strength increase with increasing strain rate but the extension at break decreased with increasing strain rate. Region 3 occurred when strain rates were greater than 280 s^{-1}. Both the tensile strength and breaking extension decreased with increasing strain rate while the initial modulus was virtually unchanged in Region 3. The deformation curve for strain rates in excess of 280 s^{-1} could also be described by a single hyperelastic curve using a third-order Ogden energy potential function.

The dynamic toughness, defined as the area under the engineering stress-strain curve, was also calculated for SBR and plotted as a function of strain rate. It was found that with increasing strain rate, the toughness increased in Region 1, remained roughly constant in Region 2, and decreased in Region 3. Several impact tensile tests were performed to show how the dynamic toughness could be used to determine failure of rubber sheets under high strain rates. In all sheet experiments, a hole first developed in the center of the sheet and the load dropped as the hole enlarged to rupture the sheet completely.

A finite element program using ABAQUS Explicit was written to show how the dynamic toughness could be used as a failure parameter in rubber sheets. A third-order Ogden strain energy function was used to describe the hyperelastic curve in Region 3 and the variation of the dynamic toughness was found with respect to the first invariant of the left Cauchy-Green strain rate tensor. Failure was said to occur in sheets when the strain energy density at center of the sheet was equal to the toughness at the same first invariant of the left Cauchy-Green strain rate tensor. This simple failure criterion based on the dynamic toughness and first invariant of the left Cauchy-Green strain rate tensor gave the breaking extension of sheets that were in close agreement with measured values. Specifically, predicted values of the sheet extension at the onset of failure using this failure criterion were within 10% of experimental values. Future research will involve the use of more advanced hyper-viscoelastic theory to model the elastomer in Regions 1 and 2.

Acknowledgements

This research was supported by NSF Grant CMS-0347042. The authors would like to thank the Akron Rubber Development Laboratory for supplying sheets

of SBR for the experiments and Motion Engineering for high-speed video photography. They also thank Dr. Joseph Padovan, Dr. Gary Hamed, Dr. Tirumalai Srivatsan, and Dr. Jon Gerhardt for their support during the experiments.

References

1. D. S. VILLARS, *J. Appl. Phys.* **21** (1950) 565.
2. M. L. DANNIS, in "High Speed Testing," edited by A. G. H. Dietz and F. R. Eirich (John Wiley & Sons, New York, 1962) Vol. 3, p. 35.
3. P. KAINRADL and F. HANDLER, *Rubber Chem. Technol.* **33** (1960) 1438.
4. H. W. GREENSMITH, *J. Appl. Polym. Sci.* **III**(8) (1960) 175.
5. S. RAO, V. P. W. SHIM and S. E. QUAH, *ibid.* **66** (1997) 619.
6. B. SONG and W. CHEN, *J. Eng. Mat. Tech.* **125** (2003) 294.
7. J. M. KELLY, in "Earthquake Resistant Design with Rubber" (Springer-Verlag, London, 1997).
8. M. L. WILLIAMS, R. F. LANDEL and J. D. FERRY, *J. Amer. Chem. Soc.* **77** (1955) 3701.
9. T. L. SMITH, *J. Polym. Sci.* **32** (1958) 99.
10. I. BEKAR, M. S. HOO FATT and J. PADOVAN, *Tire Sci. Technol.* **30**(1) (2002) 45.
11. I. BEKAR, Doctoral Thesis, The University of Akron, August 2003.
12. ASTM, in "Annual Book of ASTM Standard," Vol. 09.01 (ASTM, 1998).
13. A. N. GENT and P. MARTENY, *J. Appl. Phys.* **53**(9) (1982) 6069.
14. T. ALFREY, in "Mechanical Behavior of High Polymers" (Interscience, New York, 1948).
15. HIBBIT, KARLSON and SORENSON INC, ABAQUS User Manual Version 6.3 (Pawtucket, RI, 2002).
16. E. M. ARRUDA and M. C. BOYCE, *J. Mech. Phys. Solids* **41**(2) (1993) 389.
17. A. N. GENT, *Rubber Chem. Technol.* **69** (1966) 59.

Received 5 December 2003
and accepted 23 June 2004